IEEE Robotics and Automation Letters (RA-L) paper, presented at ICRA 2024, Yokohama, Japan. Cite as RA-L paper.

# Aerial Physical Human Robot Interaction for Payload Transportation

Pratik Prajapati, and Vineet Vashista

***Abstract*—Recent human-robot interaction paradigms on aerial robots unfold many potential applications, and efforts are further being made to explore this field. Physical interaction with aerial robots can provide an intuitive way of delivering high-level commands and allowing humans to perform collaborative tasks. The presented work demonstrates the feasibility of deploying the aerial robot to physically work with the human operator to transport the payload collaboratively in outdoor settings. A system comprised of a rigid object lifted by a human and a quadcopter from its end is considered. Custom build sensor systems, namely Human Handle Device and Cable Attitude Device, have been designed to estimate human commands and state feedback reliably. A control strategy for the quadcopter is designed to interact naturally with the operator for safer and smooth collaborative payload transportation. Successful outdoor experiments with five novice subjects are presented that demonstrate the feasibility and potential application of the proposed modality.**

***Index Terms*—Physical Human-Robot Interaction, Aerial Systems: Mechanics and Control, Aerial Systems: Applications**

## I. INTRODUCTION

HUMAN-robot interaction (*HRI*) paradigm has been effectively utilized in augmenting robots' operational capabilities by human commands to accomplish desired performance during complex tasks, such as robotic surgery, remote object handling, and visual telemanipulation [1]. In such operations, humans use their cognitive abilities to supply high-level control commands to the robots based on available sensory information and external conditions. The robots compute low-level control actions to perform various critical actions. Robots that have been extensively used for such paradigms include mobile robots, serial-chain robots, and exoskeletons [2]–[4].

Teleoperation of aerial robots by human operators is among the most frequently and successfully implemented *HRI* paradigms in the literature [5]–[13]. The teleoperation paradigm has been used for both exclusive flying applications, such as aerial exploration, surveillance, photography, etc. [5], [6], as well as for applications requiring an aerial robot's physical interaction with the environment, such as aerial grasping [7], physical inspection [8], manipulation [9], and payload transportation [10]–[13].

Manuscript received: December, 22, 2022; Revised March, 31, 2023; Accepted June, 01, 2023. This paper was recommended for publication by Editor Pauline Pounds upon evaluation of the Associate Editor and Reviewers' comments. This work was supported by Core Research Grant (CRG/2020/004990) from SERB India. (*Corresponding author: Vineet Vashista*)

Pratik Prajapati and Vineet Vashista are with the Human-Centered Robotics lab at IIT Gandhinagar, Gandhinagar, Gujarat 382055, India (e-mail: pratik.prajapati@iitgn.ac.in; vineet.vashista@iitgn.ac.in)

Digital Object Identifier (DOI): see top of this page.

With the ongoing technological advancement, the design and control of aerial robots have evolved significantly not only to improve their flight time, flight quality, and dynamic capabilities but also to make their operation safer, easier, and more reliable. Features including the addition of propeller guards and protective cage surrounding the chassis [14], [15] make the aerial robots crashproof. Moreover, control architectures based on the admittance control have been developed [16]–[19], where defining apparent stiffness, inertia, and damping to aerial robot enable a natural way of interaction with the surrounding. These efforts have enabled medium size aerial robots, such as quadcopters, to operate close to the human workspace during a flying task. Thereby enabling physical interaction with aerial robots as an alternate mode of delivering high-level commands.

Works in [16]–[21] demonstrate some unique physical human aerial robot interaction (*pHARI*) paradigms. In [16], a human operator acts as a high-level motion planner to physically guide a quadcopter's motion while transporting a foam brick. A slung load system lifted by five aerial vehicles is demonstrated in [18] where the user directs the motion of the system by haptic interaction. More recently [21], a safety-aware control paradigm has been shown where human operators physically manipulate and guide the motion of the payload transported by three quadcopters. An admittance-based control framework to control an aerial manipulator in a simulated environment is presented in [20]. Contrary to these works, where a human guides the system's motion, the works in [17], [19] deployed *pHARI* paradigms to assist the human. Specifically, a quadcopter is programmed to apply external force perturbations via a tether to direct a human in moving along the desired path.

The above *pHARI* paradigms distinctively establish applications where a human operator either guides the system or be led by aerial robots [16]–[21]. However, the human operator interacts by only applying external forces to the aerial robotic system, which is self-sustained and does not require continuous human input. The usefulness of a *pHARI* modality can further be extended by making the human operator part of the aerial system, where the operator and aerial robot physically collaborate to perform a common task. The merits of such human-robot cooperative tasks have been demonstrated in literature but with ground robots, for example, an assistive manipulator cut a beam of wood with a human [22], and a humanoid transport a bulky table with a human [23].

In this context, the current work presents a *pHARI* modality to execute a physical task collaboratively in outdoor settings. The problem of collaborative transportation of a rigid payload

IEEE Robotics and Automation Letters (RA-L) paper, presented at ICRA 2024, Yokohama, Japan. Cite as RA-L paper.

**IEEE Robotics and Automation Letters (RA-L) paper, presented at ICRA 2024, Yokohama, Japan. Cite as RA-L paper.**

by a human and a quadcopter is considered. The human operator does not fly the system but lifts the payload at one end and maneuvers it along a path. The quadcopter lifts the other end of the payload and is controlled to achieve a safe and smooth collaborative payload transportation. An outdoor human-quadcopter experiment with five novice subjects is presented to demonstrate the feasibility of the work.

## II. METHODS

Figure 1 shows the experimental setup of the proposed *pHARI* paradigm for collaborative aerial transportation of a payload by a human operator and a quadcopter in outdoor settings. A cross configuration quadcopter of frame size *F*450 (the distance between two diagonal motors is 450 mm) is used. An open-source Pixhawk autopilot is used as the flight controller of the quadcopter. The human operator grabs Human Handle Device (*HHD*) from its base, and a clamp is fitted at the end to grasp the payload, as shown in Figs. 1 & 3. A safety switch is provided on top of the *HHD* to arm and disarm the quadcopter for safely take off and land the quadcopter at the human operator's convenience. A hollow steel rod of 1.8 cm in diameter and weight of 0.26 kg is used as a payload. A Cable Attitude Measurement Device (*CAMD*) is attached underneath the quadcopter to lift the other end of the payload using an inextensible cable. The design and operation of *HHD* and *CAMD* are discussed in Sec. III. The physical parameters of the experimental setup are listed in Table I.

| Description | Notation | Value |
|---|---|---|
| Mass of quadcopter | $m_q$ | 1.236 kg |
| Mass of payload | $m_p$ | 0.26 kg |
| MOI of quadcopter | $\boldsymbol{J_q}$ | (1.13, 1.33, 1.87) $\times 10^{-2}$ kgm$^2$ |
| Length of payload | $2l_p$ | 1.24 m |
| Length of cable | $l_c$ | 0.3 m |

TABLE I
PHYSICAL PARAMETERS OF THE EXPERIMENTAL SETUP

### A. Dynamical Model

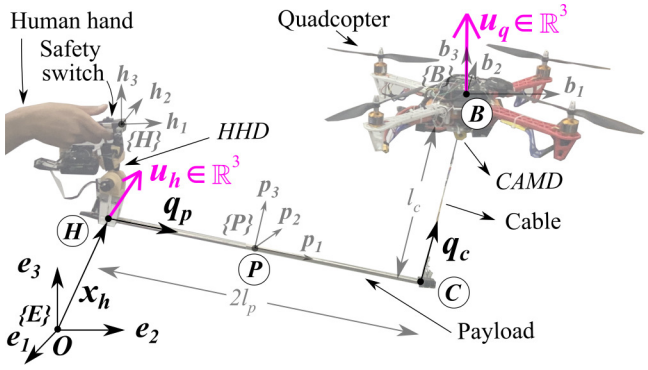


Fig. 1. The experimental setup of the proposed *pHARI* paradigm includes a cylindrical-shaped rigid payload being lifted by a human operator on one end via the *HHD* and a quadcopter at the other end via an inextensible cable attached to the *CAMD*.

The dynamic model of the system in Fig. 1 is formulated in an inertial reference frame, $\{\boldsymbol{E}\}$, located at ground with third axis, $\boldsymbol{e_3}$, vertically upward. Further, local reference frames $\{\boldsymbol{P}\}$ and $\{\boldsymbol{B}\}$ are defined for the payload and quadcopter at their geometric centers, i.e., points $\boldsymbol{P}$ and $\boldsymbol{B}$ respectively. For these frames, the $\boldsymbol{p_1}$ axis is defined longitudinally along the payload, and the $\boldsymbol{b_3}$ axis is taken normal to the quadcopter's chassis, refer to Fig. 1. A local reference frame $\{\boldsymbol{H}\}$ is also defined for the *HHD* with $\boldsymbol{h_1}$ axis along the *HHD*'s base, refer to Figs. 1 & 3. Further, $2l_p \in \mathbb{R}$ and $l_c \in \mathbb{R}$ denote the payload and cable lengths, respectively. Symbols $m_p \in \mathbb{R}$, $m_q \in \mathbb{R}$, and $\boldsymbol{J_q} \in \mathbb{R}^{3\times3}$ denote the payload mass, quadcopter mass, and quadcopter's moment of inertia about its geometric center respectively.

Consider that a cylindrical-shaped rigid payload is being lifted at its two endpoints, i.e., point $\boldsymbol{H}$ by the human operator and point $\boldsymbol{C}$ by the quadcopter, refer to Fig. 1. Thereby, the payload's attitude is defined in the 2-sphere as $\boldsymbol{q_p} \in \mathbb{S}^2$, $\mathbb{S}^2 \triangleq \{\boldsymbol{q} \in \mathbb{R}^3 | \ \|\boldsymbol{q}\|_2 = 1\}$ in frame $\{\boldsymbol{E}\}$, where $\|\cdot\|_2$ represents the second norm. Further, considering that the cable remains taut during the flight, its attitude is also defined in 2-sphere as $\boldsymbol{q_c} \in \mathbb{S}^2$. Denoting the position of point $\boldsymbol{H}$ as $\boldsymbol{x_h} \in \mathbb{R}^3$ in $\{\boldsymbol{E}\}$, the position of geometric centers of payload, $\boldsymbol{x_p} \in \mathbb{R}^3$, and quadcopter, $\boldsymbol{x_q} \in \mathbb{R}^3$, are computed as in Eq. (1). The quadcopter's attitude is represented as a rotation matrix $\boldsymbol{R_q} \in SO(3)$, $SO(3) \triangleq \{\boldsymbol{R} \in \mathbb{R}^{3\times3} | \ \boldsymbol{RR}^T = \boldsymbol{I}_{3\times3}, det(\boldsymbol{R}) = +1\}$. Defining the angular velocities of the payload, cable, and quadcopter as $\boldsymbol{\omega_p}$, $\boldsymbol{\omega_c}$, and $\boldsymbol{\Omega_q}$ respectively, the kinematic relations for the attitude of payload, cable, and quadcopter are written in Eq. (2). Here, the *hatmap* $\widehat{\cdot}: \mathbb{R}^3 \to so(3)$ is defined as $\widehat{\boldsymbol{x}}\boldsymbol{y} = \boldsymbol{x} \times \boldsymbol{y}$ for all $\boldsymbol{x}, \boldsymbol{y} \in \mathbb{R}^3$, where $so(3)$ is the skew-symmetric matrix.

$$\boldsymbol{x_p} = \boldsymbol{x_h} + l_p\boldsymbol{q_p}, \quad \boldsymbol{x_q} = \boldsymbol{x_h} + 2l_p\boldsymbol{q_p} + l_c\boldsymbol{q_c} \tag{1}$$

$$\dot{\boldsymbol{q}}_{\boldsymbol{p}} = \boldsymbol{\omega_p} \times \boldsymbol{q_p}, \ \ \dot{\boldsymbol{q}}_{\boldsymbol{c}} = \boldsymbol{\omega_c} \times \boldsymbol{q_c}, \ \ \dot{\boldsymbol{R}}_{\boldsymbol{q}} = \boldsymbol{R_q}\widehat{\boldsymbol{\Omega}}_{\boldsymbol{q}} \tag{2}$$

$$\boldsymbol{u_q} = f\boldsymbol{R_q}\boldsymbol{e_3} \tag{3}$$

To develop the equations of motion (*EOM*) for the collaborative transportation of the payload, the effect of human operator's actions on the payload is modeled by an interactive force, denoted as $\boldsymbol{u_h} \in \mathbb{R}^3$ at point $\boldsymbol{H}$ in $\{\boldsymbol{E}\}$ as shown in Fig. 1. Similarly, the effect of the quadcopter during the transportation task is modeled as a force vector $\boldsymbol{u_q} \in \mathbb{R}^3$ at point $\boldsymbol{B}$ in $\{\boldsymbol{E}\}$. Denoting the resultant thrust force and moment generated by the quadcopter as $f \in \mathbb{R}$ along $\boldsymbol{b_3}$ and $\boldsymbol{M_q} \in \mathbb{R}^3$ about $\boldsymbol{b_1}, \boldsymbol{b_2}$, and $\boldsymbol{b_3}$ respectively, the force vector $\boldsymbol{u_q}$ is defined by the components of thrust force $f$ along $\boldsymbol{e_1}$, $\boldsymbol{e_2}$, and $\boldsymbol{e_3}$ as given in Eq. (3). Using the Lagrange-d'Alembert principle on a manifold [24], *EOM* of the system are derived and given in Eqs. (4 & 5). Here, $m_1 = (m_q + m_p)$, $m_2 = (2m_q + m_p)$, $m_3 = (4m_q + \frac{4}{3}m_p)$, $m_4 = 2m_q l_p l_c$.

$$\begin{bmatrix} m_1\boldsymbol{I}_3 & -m_2 l_p\widehat{\boldsymbol{q}}_{\boldsymbol{p}} & -m_q l_c\widehat{\boldsymbol{q}}_{\boldsymbol{c}} \\ -m_2 l_p\widehat{\boldsymbol{q}}_{\boldsymbol{p}} & m_3 l_p^2\widehat{\boldsymbol{q}}_{\boldsymbol{p}}^{\boldsymbol{2}} & m_4\widehat{\boldsymbol{q}}_{\boldsymbol{p}}\widehat{\boldsymbol{q}}_{\boldsymbol{c}} \\ -m_q l_c\widehat{\boldsymbol{q}}_{\boldsymbol{c}} & m_4\widehat{\boldsymbol{q}}_{\boldsymbol{c}}\widehat{\boldsymbol{q}}_{\boldsymbol{p}} & m_q l_c^2\widehat{\boldsymbol{q}}_{\boldsymbol{c}}^{\boldsymbol{2}} \end{bmatrix} \begin{bmatrix} \ddot{\boldsymbol{x}}_{\boldsymbol{h}} \\ \dot{\boldsymbol{\omega}}_{\boldsymbol{p}} \\ \dot{\boldsymbol{\omega}}_{\boldsymbol{c}} \end{bmatrix} + \begin{bmatrix} -m_2 l_p\widehat{\dot{\boldsymbol{q}}}_{\boldsymbol{p}}\boldsymbol{\omega_p} - m_q l_c\widehat{\dot{\boldsymbol{q}}}_{\boldsymbol{c}}\boldsymbol{\omega_c} + m_1 g\boldsymbol{e_3} \\ m_3 l_p^2\widehat{\boldsymbol{q}}_{\boldsymbol{p}}\widehat{\dot{\boldsymbol{q}}}_{\boldsymbol{p}}\boldsymbol{\omega_p} + m_4\widehat{\boldsymbol{q}}_{\boldsymbol{p}}\widehat{\dot{\boldsymbol{q}}}_{\boldsymbol{c}}\boldsymbol{\omega_c} - m_2 l_p g\widehat{\boldsymbol{q}}_{\boldsymbol{p}}\boldsymbol{e_3} \\ m_q l_c^2\widehat{\boldsymbol{q}}_{\boldsymbol{c}}\widehat{\dot{\boldsymbol{q}}}_{\boldsymbol{c}}\boldsymbol{\omega_c} + m_4\widehat{\boldsymbol{q}}_{\boldsymbol{c}}\widehat{\dot{\boldsymbol{q}}}_{\boldsymbol{p}}\boldsymbol{\omega_p} - m_q l_c g\widehat{\boldsymbol{q}}_{\boldsymbol{c}}\boldsymbol{e_3} \end{bmatrix} = \begin{bmatrix} \boldsymbol{u_q} + \boldsymbol{u_h} \\ -2l_p\widehat{\boldsymbol{q}}_{\boldsymbol{p}}\boldsymbol{u_q} \\ -l_c\widehat{\boldsymbol{q}}_{\boldsymbol{c}}\boldsymbol{u_q} \end{bmatrix} \tag{4}$$

$$\boldsymbol{J_q}\dot{\boldsymbol{\Omega}}_{\boldsymbol{q}} + \widehat{\boldsymbol{\Omega}}_{\boldsymbol{q}}\boldsymbol{J_q}\boldsymbol{\Omega_q} = \boldsymbol{M_q} \tag{5}$$

**IEEE Robotics and Automation Letters (RA-L) paper, presented at ICRA 2024, Yokohama, Japan. Cite as RA-L paper.**

### *B. Collaborative Payload Transportation Formulation*

The focus of the presented work is to enable a quadcopter to interact physically with a human operator to execute collaborative payload transportation in outdoor settings. As part of the proposed formulation, a human operator is tasked with high-level decision-making to plan a path for the system to move along, which is referred to as desired path $\boldsymbol{x_{h_d}} \in \mathbb{R}^3$. The human operator commands the system by exerting an interaction force, modeled as force vector $\boldsymbol{u_h}$ at one end of the payload, which also serves to lift a part weight of the payload. To execute this physical human aerial robot interaction (*pHARI*) along $\boldsymbol{x_{h_d}}$ successfully, the quadcopter is controlled to generate a force vector $\boldsymbol{u_q}$ that maintains the cable and payload in particular attitudes, say $\boldsymbol{q_{c_d}} \in \mathbb{S}^2$ and $\boldsymbol{q_{p_d}} \in \mathbb{S}^2$, respectively. The presented implementation intends to keep the cable vertically taut during flight, i.e., $\boldsymbol{q_{c_d}} = \boldsymbol{e_3}$. In contrast, the payload attitude is accepted to change during flight and is taken as $\boldsymbol{q_{p_d}} = \boldsymbol{h_1}$. Essentially, the human operator adjudges $\boldsymbol{q_{p_d}}$ on the go using the *HHD*. Such manifestation allows the operator to execute diverse trajectories for navigation in a real-world layout without onboard localization. Furthermore, equal payload weight sharing between human and quadcopter is sought, such that desired values of $\boldsymbol{u_h}$ and $\boldsymbol{u_q}$, i.e., $\boldsymbol{u_{h_d}}$ and $\boldsymbol{u_{q_d}}$ are defined as given in Eq. (6). Lastly, to control the payload's and cable's oscillations during flight, the desired angular velocities and attitude rates are set at zero, i.e., $\boldsymbol{\omega_{p_d}} = \boldsymbol{\omega_{c_d}} = \boldsymbol{0_{3\times1}}$, and $\dot{\boldsymbol{q}}_{\boldsymbol{p_d}} = \dot{\boldsymbol{q}}_{\boldsymbol{c_d}} = \boldsymbol{0_{3\times1}}$ respectively.

$$\boldsymbol{u_{h_d}} = (m_p/2)g\boldsymbol{e_3}, \quad \boldsymbol{u_{q_d}} = (m_q + (m_p/2))g\boldsymbol{e_3} \tag{6}$$

### *C. Quadcopter Controller Design*

As part of the proposed collaborative strategy, the quadcopter applies a force vector $\boldsymbol{u_q}$ that, i) supports payload's half weight in addition to its own weight, i.e., $\boldsymbol{u_{q_d}}$ in Eq. (6), and ii) maintains the desired cable and payload attitudes, $\boldsymbol{q_{c_d}}$ and $\boldsymbol{q_{p_d}}$. The current work implements the required $\boldsymbol{u_q}$ through attitude and altitude controllers of the quadcopter, such that it generates a thrust force $f = \|\boldsymbol{u_q}\|_2$ and moment $\boldsymbol{M_q}$ that orients the quadcopter into the desired attitude $\boldsymbol{R_{q_d}}$ to satisfy Eq. (3). Accordingly, the system dynamics are linearized about the desired configuration, and a state-feedback control law is implemented as described below.

*Linearization:* Variation-based linearization [25] of system dynamics in Eq. (4) is performed to obtain the linearized model given in Eq. (7) with state-vector, $\boldsymbol{\delta s} \in \mathbb{R}^{16}$, and control-vector, $\boldsymbol{\delta u} \in \mathbb{R}^6$, as defined in Eqs. (8 & 9) respectively. Expressions for matrices $\boldsymbol{M} \in \mathbb{R}^{16\times16}$, $\boldsymbol{N} \in \mathbb{R}^{16\times6}$, and $L \in \mathbb{R}^{3\times2}$ are given in Appendix V-A.

$$\textit{State-space model: } \boldsymbol{\delta \dot{s}} = \boldsymbol{M\delta s} + \boldsymbol{N\delta u} \tag{7}$$

$$\textit{State vector: } \boldsymbol{\delta s} = \begin{bmatrix} \boldsymbol{\delta x_h^T} & \boldsymbol{\xi_p^T} & \boldsymbol{\xi_c^T L} & \boldsymbol{\delta \dot{x}_h^T} & \boldsymbol{\delta \omega_p^T} & \boldsymbol{\delta \omega_c^T L} \end{bmatrix}^T \tag{8}$$

$$\textit{Control input: } \boldsymbol{\delta u} = \begin{bmatrix} \boldsymbol{\delta u_h^T} & \boldsymbol{\delta u_q^T} \end{bmatrix}^T \tag{9}$$

The position and velocity of payload, represented by endpoint $\boldsymbol{H}$ in Fig. 1, and the interaction force vectors, $\boldsymbol{u_h}$ and $\boldsymbol{u_q}$, evolve on euclidean space, i.e., $\{\boldsymbol{x_h}, \dot{\boldsymbol{x}}_{\boldsymbol{h}}, \boldsymbol{u_h}, \boldsymbol{u_q}\} \in \mathbb{R}^3$. Suitably, their variations are defined as per Eqs. (10 & 11), respectively. As the payload and cable attitude evolve on $\mathbb{S}^2$ and any curve on $\mathbb{S}^2$ can be $\epsilon$-parameterized using exponential map [24] as in Eq. (12), their variations are defined as per Eq. (13). Here, $\epsilon \in (-c, c)$ with $c > 0$ and $\boldsymbol{\xi_{(\cdot)}} \in \mathbb{R}^3$ is a differentiable curve such that $\boldsymbol{\xi_{(\cdot)}} \cdot \boldsymbol{q_{(\cdot)_d}} = 0$. The subscript $(\cdot) \in \{c, p\}$, where the letters $c$ and $p$ are used to represent cable and payload, respectively. Considering that the current and desired attitudes are closer, the values of $\boldsymbol{\xi_{(\cdot)}}$ and the variation in the angular velocity, $\boldsymbol{\delta\omega_{(\cdot)}}$, are approximated as the errors on $\mathbb{S}^2$, i.e., $\boldsymbol{e_{q_{(\cdot)}}}$ and $\boldsymbol{e_{\omega_{(\cdot)}}}$ respectively as given in Eq. (14). Here, $\boldsymbol{q_{(\cdot)_d}}$ and $\boldsymbol{\omega_{(\cdot)_d}}$ are the desired attitude and angular velocity.

$$\boldsymbol{\delta x_h} = \boldsymbol{x_h} - \boldsymbol{x_{h_d}}, \quad \boldsymbol{\delta \dot{x}_h} = \dot{\boldsymbol{x}}_{\boldsymbol{h}} - \dot{\boldsymbol{x}}_{\boldsymbol{h_d}} \tag{10}$$

$$\boldsymbol{\delta u_h} = \boldsymbol{u_h} - \boldsymbol{u_{h_d}}, \quad \boldsymbol{\delta u_q} = \boldsymbol{u_q} - \boldsymbol{u_{q_d}} \tag{11}$$

$$\boldsymbol{q_{(\cdot)}^{\epsilon}} = exp(\epsilon \hat{\boldsymbol{\xi}}_{(\cdot)})\boldsymbol{q_{(\cdot)_d}} \tag{12}$$

$$\boldsymbol{\delta q_{(\cdot)}} = \frac{d}{d\epsilon}\boldsymbol{q_{(\cdot)}^{\epsilon}}\bigg|_{\epsilon=0} = \boldsymbol{\xi_{(\cdot)}} \times \boldsymbol{q_{(\cdot)_d}} \tag{13}$$

$$\boldsymbol{\xi_{(\cdot)}} \approx \boldsymbol{e_{q_{(\cdot)}}} = \widehat{\boldsymbol{q}}_{(\cdot)_d}\boldsymbol{q_{(\cdot)}}, \quad \boldsymbol{\delta\omega_{(\cdot)}} \approx \boldsymbol{e_{\omega_{(\cdot)}}} = \boldsymbol{\omega_{(\cdot)}} - (-\widehat{\boldsymbol{q}}_{(\cdot)}^2)\boldsymbol{\omega_{(\cdot)_d}} \tag{14}$$

*State-feedback control law:* A state-feedback control law, as per Eq. (15), is designed for the control input, $\boldsymbol{\delta u}$, of the linearized model Eq. (7). Accordingly, the closed loop linearized model is written in Eq. (16). As per the collaborative payload transportation strategy, the quadcopter is mainly tasked with controlling the cable and payload attitude, i.e., $\boldsymbol{q_c}$, and $\boldsymbol{q_p}$. Accordingly, the state-feedback gain matrix for quadcopter, $\boldsymbol{\mathcal{K}_q} \in \mathbb{R}^{3\times16}$, is designed with zero values corresponding to $\boldsymbol{\delta x_h}$ and $\boldsymbol{\delta \dot{x}_h}$ states as in Eq. (18). In contrast, the human operator makes higher-level decisions to plan and navigate the payload at the desired path. Thus, as per the formulated state-feedback control law, it is interpreted that the inputs supplied by the human operator, $\boldsymbol{\delta u_h}$, are mainly to control the states $\boldsymbol{\delta x_h}$ and $\boldsymbol{\delta \dot{x}_h}$. Accordingly, the state-feedback gain matrix corresponding to the human operator, $\boldsymbol{\mathcal{K}_h} \in \mathbb{R}^{3\times16}$, comprises zero values for states other than $\boldsymbol{\delta x_h}$ and $\boldsymbol{\delta \dot{x}_h}$ as in Eq. (17).

$$\boldsymbol{\delta u} = \begin{bmatrix} \boldsymbol{\delta u_h} \\ \boldsymbol{\delta u_q} \end{bmatrix} = -\begin{bmatrix} \boldsymbol{\mathcal{K}_h} \\ \boldsymbol{\mathcal{K}_q} \end{bmatrix} \boldsymbol{\delta s} = -\boldsymbol{\mathcal{K}\delta s} \tag{15}$$

$$\boldsymbol{\delta \dot{s}} = (\boldsymbol{M} - \boldsymbol{N\mathcal{K}})\boldsymbol{\delta s} \tag{16}$$

$$\boldsymbol{\mathcal{K}_h} = \begin{bmatrix} \boldsymbol{\mathcal{K}_{x_h}} & \boldsymbol{0_{3\times3}} & \boldsymbol{0_{3\times2}} & \boldsymbol{\mathcal{K}_{\dot{x}_h}} & \boldsymbol{0_{3\times3}} & \boldsymbol{0_{3\times2}} \end{bmatrix} \tag{17}$$

$$\boldsymbol{\mathcal{K}_q} = \begin{bmatrix} \boldsymbol{0_{3\times3}} & \boldsymbol{\mathcal{K}_{q_p}} & \boldsymbol{\mathcal{K}_{q_c}} & \boldsymbol{0_{3\times3}} & \boldsymbol{\mathcal{K}_{\omega_p}} & \boldsymbol{\mathcal{K}_{\omega_c}} \end{bmatrix} \tag{18}$$

Extensive experimental trials were conducted with the setup to tune the state feedback gain matrix for quadcopter, $\boldsymbol{\mathcal{K}_q}$. Specifically, a diverse range of perturbations was applied at point $\boldsymbol{H}$ via *HHD* with varying desired payload attitudes while managing a good tracking of desired cable and payload attitude. These trials were conducted to represent the cases where a human operator maneuvers the payload steadily, i.e., with no abrupt commands, such that the values of $\boldsymbol{\mathcal{K}_h}$ were presumed bounded. Accordingly, the proposed state feedback law implemented a stable human-quadcopter collaborative payload transportation.

*Quadcopter's Altitude controller:* Using Eqs. (6, 11, & 15), the value of $\boldsymbol{u_q}$ is found out as given in Eq. (19). The altitude

**IEEE Robotics and Automation Letters (RA-L) paper, presented at ICRA 2024, Yokohama, Japan. Cite as RA-L paper.**

**IEEE Robotics and Automation Letters (RA-L) paper, presented at ICRA 2024, Yokohama, Japan. Cite as RA-L paper.**

controller to generate the total thrust force $f$ by the quadcopter is found out using Eq. (20).

$$\boldsymbol{u_q} = -\boldsymbol{\mathcal{K}_q}\boldsymbol{\delta s} + (m_q + (m_p/2))g\boldsymbol{e_3} \tag{19}$$

$$f = \|\boldsymbol{u_q}\|_2 \tag{20}$$

*Quadcopter's Attitude controller:* The quadcopter's attitude controller is designed to control its orientation, $\boldsymbol{R_q}$, such that the components of thrust force $f$ in frame $\{\boldsymbol{E}\}$ equals $\boldsymbol{u_q}$ as to satisfy Eq. (3). This is achieved by taking the desired third axis of the quadcopter, $\boldsymbol{b_{3_d}}$, along the unit vector $\boldsymbol{u_q}$, as defined in Eq. (21). The other two axes are considered such that the first axis of the payload, $\boldsymbol{p_1}$, lies in the plane formed by the axes $\boldsymbol{b_{1_d}}$ and $\boldsymbol{b_{3_d}}$ to yield the desired quadcopter's attitude, $\boldsymbol{R_{q_d}}$, as in Eq. (21). Such an implementation makes it easier for the human operator to judge the quadcopter's orientation. Accordingly, the geometric attitude controller [26] is utilized to track $\boldsymbol{R_{q_d}}$ as illustrated in Eq. (22).

$$\boldsymbol{R_{q_d}} = \Big[\ \underbrace{\boldsymbol{b_{2_d}} \times \boldsymbol{b_{3_d}}}_{\boldsymbol{b_{1_d}}}\quad \underbrace{\boldsymbol{b_{3_d}} \times \boldsymbol{p_1}}_{\boldsymbol{b_{2_d}}}\quad \underbrace{\frac{\boldsymbol{u_q}}{\|\boldsymbol{u_q}\|_2}}_{\boldsymbol{b_{3_d}}}\ \Big] \in SO(3) \tag{21}$$

$$\begin{aligned}\boldsymbol{M_q} = &-\boldsymbol{k_{R_q}}\boldsymbol{e_{R_q}} - \boldsymbol{k_{\Omega_q}}\boldsymbol{e_{\Omega_q}} + \boldsymbol{\Omega_q} \times \boldsymbol{J_q}\boldsymbol{\Omega_q} \\ &- \boldsymbol{J_q}(\widehat{\boldsymbol{\Omega}}_{\boldsymbol{q}}\boldsymbol{R_q^T}\boldsymbol{R_{q_d}}\boldsymbol{\Omega_{q_d}} - \boldsymbol{R_q^T}\boldsymbol{R_{q_d}}\dot{\boldsymbol{\Omega}}_{\boldsymbol{q_d}})\end{aligned} \tag{22}$$

The gain matrices $\boldsymbol{k_{R_q}}$ and $\boldsymbol{k_{\Omega_q}}$ are tuned to get desired attitude response of the quadcopter. The errors in the quadcopter's attitude and angular velocity are found out as $\boldsymbol{e_{R_q}} = \frac{1}{2}(\boldsymbol{R_{q_d}^T}\boldsymbol{R_q} - \boldsymbol{R_q^T}\boldsymbol{R_{q_d}})^\vee, \boldsymbol{e_{\Omega_q}} = \boldsymbol{\Omega_q} - \boldsymbol{R_q^T}\ \boldsymbol{R_{q_d}}\boldsymbol{\Omega_{q_d}}$ [26], and *veemap* $(\cdot)^\vee : so(3) \rightarrow \mathbb{R}^3$.

## III. OUTDOOR EXECUTION

### A. Implementation of Proposed Collaborative Strategy

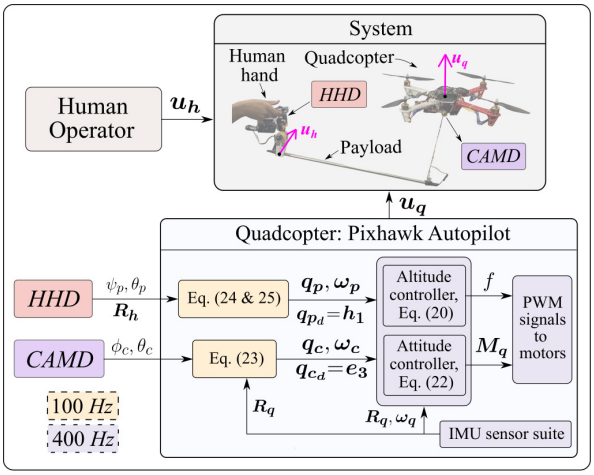


Fig. 2. Overall control architecture of the presented *pHARI* paradigm. Human operator supplies $\boldsymbol{u_h}$ force vector to navigate the payload at desired path. Computation of thrust force, $f$, and moment, $\boldsymbol{M_q}$, to be generated by the quadcopter is done onboard autopilot. Respective PWM signals are supplied to the motors such that the quadcopter generates $\boldsymbol{u_q}$ force vector.

The overall control architecture of the presented *pHARI* is shown in Fig. 2. The human operator grabs the payload from one end using *HHD* and applies $\boldsymbol{u_h}$ force vector to control the motion of the payload's position, i.e., $\boldsymbol{x_h}$. The proposed *pHARI* paradigm can be implemented in the outdoor settings knowing the real-time feedback of payload's and cable's attitudes and their time rates, i.e., $\boldsymbol{q_p}, \boldsymbol{q_c}, \boldsymbol{\omega_p}$, and $\boldsymbol{\omega_c}$, as required by the quadcopter's altitude controller in Eq. (20). Accordingly, Human Handle Device (*HHD*) and Cable Attitude Measurement Device (*CAMD*) have been designed and used in the current work, as described below. The real-time data captured by *HHD* and *CAMD* are transferred to the quadcopter's autopilot using UART communication at $100Hz$ to estimate the cable's and payload's attitude and angular velocity, i.e., $(\boldsymbol{q_c}, \boldsymbol{\omega_c})$ and $(\boldsymbol{q_p}, \boldsymbol{\omega_p})$, respectively. Autopilot's onboard IMU sensor suite is used to get the feedback of the quadcopter's attitude and angular velocity, i.e., $\boldsymbol{R_q}$ and $\boldsymbol{\omega_q}$, respectively. The customized algorithms are written in ardupilot firmware to implement altitude and attitude controller at $400Hz$, i.e., Eqs. (20 & 22). The motor's thrust and moment characteristics w.r.t. PWM signals are estimated using an in-house lab facility. Finally, specific PWM signals are supplied to the motors to generate required values of $f$ and $\boldsymbol{M_q}$ such that the quadcopter supplies $\boldsymbol{u_q}$ force vector for successful collaborative transportation as shown in Fig. 2.

### B. Estimation of $\boldsymbol{q_c}$ and $\boldsymbol{\omega_c}$

*CAMD*, as shown in Fig. 3 (a), is designed similar in function to a joystick to estimate the cable attitude and its rate as demonstrated previously [10]. It consists of two orthogonal shafts. One of the shafts has a circular slot through which the second shaft passes and is pivoted to a lever. The *CAMD* lever is connected to the payload via a cable, such that any change in cable attitude results in the rotation of the two shafts. A coordinate frame $\{\boldsymbol{C}\}$ is defined for *CAMD* with $\boldsymbol{c_1}$ and $\boldsymbol{c_2}$ axes aligned along the shafts. The shafts are fitted with rotary magnetic encoders connected with a microcontroller, NodeMCU, to record the angular positions $\phi_c$ and $\theta_c$ about $\boldsymbol{c_1}$ and $\boldsymbol{c_2}$ axes, respectively.

*CAMD* is mounted rigidly underneath the quadcopter, refer to Fig. 1, such that $\boldsymbol{b_3}$ coincides $\boldsymbol{c_3}$, and $\boldsymbol{c_1}$ and $c_2$ are parallel to $\boldsymbol{b_1}$ and $\boldsymbol{b_2}$, respectively. Thus, angular positions measured by *CAMD* are in the quadcopter's body frame $\{\boldsymbol{B}\}$. Accordingly, cable's attitude in inertial frame $\{\boldsymbol{E}\}$ is computed as in Eq. (23) knowing the quadcopter's attitude, $\boldsymbol{R_q}$, from the IMU sensor suite of the onboard autopilot. Using kinematic relations of Eq. (2), $\boldsymbol{\omega_c}$ is calculated as per Eq. (23). Matrices $\boldsymbol{R_1}(\cdot)$ and $\boldsymbol{R_2}(\cdot)$ represent standard rotation matrices about first and second axes respectively [27].

$$\boldsymbol{q_c} = \boldsymbol{R_q}\boldsymbol{R_1}(\phi_c)\boldsymbol{R_2}(\theta_c)\boldsymbol{e_3}, \quad \boldsymbol{\omega_c} = \boldsymbol{q_c} \times \dot{\boldsymbol{q}}_{\boldsymbol{c}} \tag{23}$$

### C. Estimation of $\boldsymbol{q_p}$ and $\boldsymbol{\omega_p}$

For the proposed modality, the human operator lifts one end of the payload through *HHD*. The *HHD*, similar in function as a universal joint, where two revolute joints are placed orthogonal to each other with axes labeled as $\boldsymbol{h_{b_2}}$ and $\boldsymbol{h_{b_3}}$, refer Fig. 3 (b). The angular positions $\theta_p$ and $\psi_p$ about $\boldsymbol{h_{b_2}}$ and $\boldsymbol{h_{b_3}}$, respectively, are measured by two rotary magnetic encoders. These angular positions define the relative motion between *HHD* base and payload and are used to estimate

**IEEE Robotics and Automation Letters (RA-L) paper, presented at ICRA 2024, Yokohama, Japan. Cite as RA-L paper.**

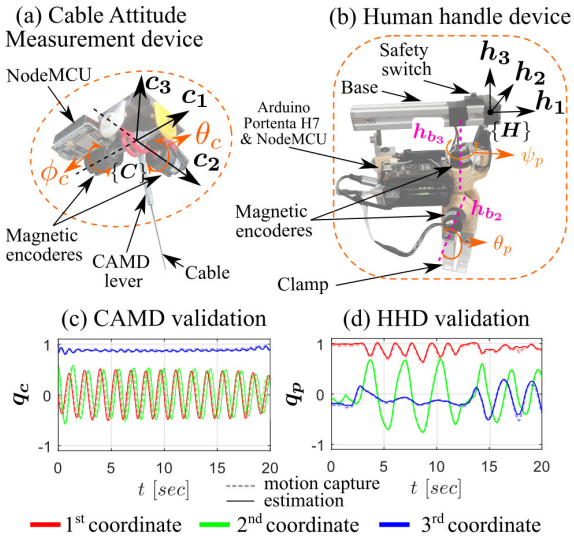


Fig. 3. Mechanical design of (a) Cable Attitude Measurement Device *(CAMD)*, and (b) Human Handle Device *(HHD)*. Plots (c) and (d) show the experimental results of *CAMD*'s and *HHD*'s validation using a motion capture system.

payload's attitude in frame $\{\boldsymbol{H}\}$, say $\boldsymbol{q_{p,\{H\}}}$, as per Eq. (24). Here, $\boldsymbol{p_1}$ is the payload's first body axis (Fig. 1). Matrix $\boldsymbol{R_3}(\cdot)$ is the standard rotation matrix about the third axis [27]. Further, an IMU unit is mounted on *HHD* base to measure its attitude in $\{\boldsymbol{E}\}$, i.e., $\boldsymbol{R_h} \in SO(3)$. The payload's attitude in $\{\boldsymbol{E}\}$ is estimated as per Eq. (25). Using kinematic relation of Eq. (2), $\boldsymbol{\omega_p}$ is calculated as in Eq. (25). Microcontrollers, Arduino Portenta and NodeMCU, are part of *HHD* to process the encoders and IMU data.

$$\boldsymbol{q_{p,\{H\}}} = \boldsymbol{R_3}(\psi_p)\boldsymbol{R_2}(\theta_p)\boldsymbol{p_1} \tag{24}$$

$$\boldsymbol{q_p} = \boldsymbol{R_h}\boldsymbol{q_{p,\{H\}}}, \quad \boldsymbol{\omega_p} = \boldsymbol{q_p} \times \dot{\boldsymbol{q}}_{\boldsymbol{p}} \tag{25}$$

### D. Validation of CAMD and HHD

Two separate lab experiments were conducted with a motion capture system that measured the ground truth values to validate the estimation of cable's and payload's attitude by devices *CAMD* and *HHD*. In the first experiment, the quadcopter chassis was mounted on a fixed frame, and a point mass was suspended underneath the quadcopter by a cable through *CAMD*. External oscillations were applied manually at the end of the cable, and the cable attitude was recorded as shown in Fig. 3 (c). In the second experiment, the point mass was replaced by a cylindrical steel rod, as in Fig. 1, with one end suspended from the quadcopter and the other end lifted by a human operator using *HHD*. The human operator applied random movements to change the payload's attitude, which was recorded as shown in Fig. 3 (d). These plots show that the estimated attitudes of cable and payload match the ground truth values measured using the motion capture system.

The errors between the estimated and ground truth data, $\boldsymbol{e_{q_{(\cdot)}}}$, were calculated using Eq. (14). For the above experiments, the root-mean-square of error magnitude in cable's and payload's attitude, $\rho(\|\boldsymbol{e_{q_{(\cdot)}}}\|)$, were 0.0548 and 0.0323, respectively. It is noted that $\rho(\|\boldsymbol{e_{q_{(\cdot)}}}\|)$ has a range from 0 to 1, which implies that the estimated attitude vector can vary from being coincident to being orthogonal to the desired attitude vector. Accordingly, the estimated cable and payload attitudes' $\rho(\|\boldsymbol{e_{q_{(\cdot)}}}\|)$ represent 5.48% and 3.23% deviations from the ground truth data, respectively. The experimental results show relatively good accuracy in cable's and payload's attitude estimation for outdoor experiments.

## IV. HUMAN-QUADCOPTER EXPERIMENTS

### A. Experiment protocol

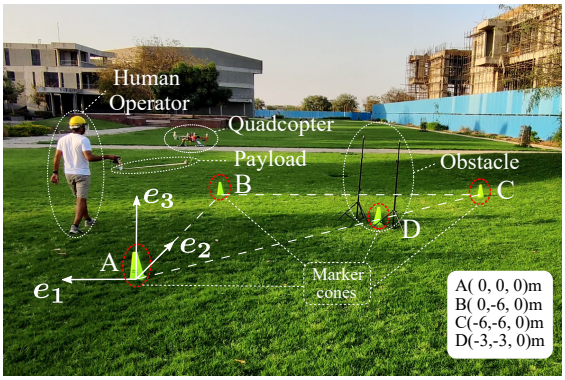


Fig. 4. Open outdoor experimental settings. Triangular-shaped cones were used as markers on the ground to indicate the path. Human operator initiate the collaborative transportation from point $\boldsymbol{A}$ and follows path $\boldsymbol{A}$-$\boldsymbol{B}$-$\boldsymbol{C}$-$\boldsymbol{A}$.

Collaborative payload transportation experiments were conducted in an open outdoor environment to demonstrate the practical implementation of the presented *pHARI* modality. A triangular-shaped path $\boldsymbol{A}$-$\boldsymbol{B}$-$\boldsymbol{C}$-$\boldsymbol{A}$, marked by cones on the ground, was considered as shown in Fig. 4. An obstacle along the middle of $\boldsymbol{AC}$ path was created using two tripods of height 1.5m, marked as point $\boldsymbol{D}$. With inertial frame at point $\boldsymbol{A}$, the locations of the points are $\boldsymbol{A}(0,0,0)$m, $\boldsymbol{B}(0,-6,0)$m, $\boldsymbol{C}(-6,-6,0)$m, and $\boldsymbol{D}(-3,-3,0)$m.

A total of five novice subjects participated in the experiment. All participants were informed about the experimental protocol and signed a written consent approved by the Institute Ethics Committee (Application No. IEC/VV/2021/011). All participants were given a demonstration on how to use the *HHD* to lift the payload, arm/disarm the quadcopter, and move the system along a path. In addition, the payload's attitude modulation while taking turns and avoiding obstacles was demonstrated through *HHD*'s base orientation. To begin the experiment, each participant hovered the system at starting point $\boldsymbol{A}$ for around two seconds. Following which the participant drove the system along $\boldsymbol{A}$-$\boldsymbol{B}$-$\boldsymbol{C}$-$\boldsymbol{A}$ path while avoiding the obstacle.

### B. Data analysis

Flight data, including $\boldsymbol{x_q}$ and $\boldsymbol{R_q}$ from quadcopter's GPS and inertial sensors, $\boldsymbol{q_c}$ from *CAMD*, and $\boldsymbol{q_p}$ and $\boldsymbol{h_1}$ from *HHD*, were logged using the data logger facility of the Pixhawk autopilot for the analysis. The human operator's position denoted by point $\boldsymbol{H}$ of *HHD*, i.e., $\boldsymbol{x_h}$, was computed using Eq. (1). As part of the proposed strategy, the human

**IEEE Robotics and Automation Letters (RA-L) paper, presented at ICRA 2024, Yokohama, Japan. Cite as RA-L paper.**

operator commands the payload attitude as $\boldsymbol{q}_{p_d} = \boldsymbol{h}_1$ and the cable attitude is defined as $\boldsymbol{q}_{c_d} = \boldsymbol{e_3}$. Thus, at any instant, the desired quadcopter's position relative to point $\boldsymbol{H}$, $\boldsymbol{x}_{q_d,H}$, can be computed as point $\boldsymbol{B}$ in blue in Fig. 5 using Eq. (1). However, using the current cable's and payload's attitude estimates in Eq. (1), the actual quadcopter's position w.r.t. point $\boldsymbol{H}$, $\boldsymbol{x}_{q,H}$, can be point $\boldsymbol{B}$ in red in Fig. 5. Therefore, the difference between the desired and actual quadcopter's positions w.r.t. point $\boldsymbol{H}$, $\boldsymbol{e}_{x_q,H} = (\boldsymbol{x}_{q_d,H} - \boldsymbol{x}_{q,H})$, was computed as a measure of the cumulative error in controlling the cable and payload attitudes simultaneously in response to human input. The errors in attitudes, $\boldsymbol{e}_{q_p}$ and $\boldsymbol{e}_{q_c}$, were also computed using Eq. (14) taking $\boldsymbol{q}_{p_d}$ and $\boldsymbol{q}_{c_d}$ as the desired attitudes. Further, the distance between the human operator and the quadcopter, $\|\boldsymbol{x}_{q,H}\|$, was considered the safety parameter for the experiment.

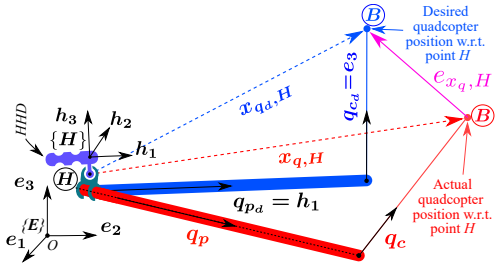


Fig. 5. Pictorial representation of the desired quadcopter's position w.r.t. point $\boldsymbol{H}$, $\boldsymbol{x}_{q_d,H}$, and the actual quadcopter's position w.r.t. point $\boldsymbol{H}$, $\boldsymbol{x}_{q,H}$. Here, $(\boldsymbol{q}_{c_d}, \boldsymbol{q}_{p_d})$ and $(\boldsymbol{q}_c, \boldsymbol{q}_p)$ denote the desired and actual attitudes (cable and payload), respectively.

### C. Experimental results

The experimental results for a representative subject and the group are shown in Figs. 6 and 7, respectively. The traversed trajectory by the system is segmented into multiple sections for better understanding. Specifically, the hovering state is labeled as $H$, a right arrow ($\rightarrow$) denotes the motion between two points, obstacle avoidance at point $\boldsymbol{D}$ is shown by an upward arrow ($\uparrow$), and turning at any point is shown as ($\circlearrowright$).

The three-dimensional trajectory plot of the representative subject (*HHD*) and the quadcopter while transporting the payload along the desired path $\boldsymbol{A}$-$\boldsymbol{B}$-$\boldsymbol{C}$-$\boldsymbol{A}$ is shown in Fig. 6 (a). Similar flights were observed for other subjects. Using *HHD*, the subject commanded the desired payload attitude as $\boldsymbol{q}_{p_d} = \boldsymbol{h}_1$, as shown in Figs. 6 (a & b). Mostly, the subject maneuvered the turns by changing the first and second coordinates of $\boldsymbol{h}_1$ and avoided the obstacle by changing the third coordinate of $\boldsymbol{h}_1$. The system responded accordingly by following the commanded $\boldsymbol{q}_{p_d}$ and achieving a successful human-quadcopter physical interaction to transport the payload along the desired path $\boldsymbol{A}$-$\boldsymbol{B}$-$\boldsymbol{C}$-$\boldsymbol{A}$.

Each participant commanded the system differently to execute the turns and obstacles. Consequently, the completion time for different sections of the trajectory was different between subjects, as reported in Fig. 7 (a). During the flight, the distance between the quadcopter and *HHD*, i.e., the safety parameter $\|\boldsymbol{x}_{q,H}\|$, was observed to closely follow the desired value $\|\boldsymbol{x}_{q_d,H}\|$, refer to Fig. 6 (f). The mean values of $\|\boldsymbol{x}_{q,H}\|$ were observed to be greater than the payload's length ($2l_p$) for

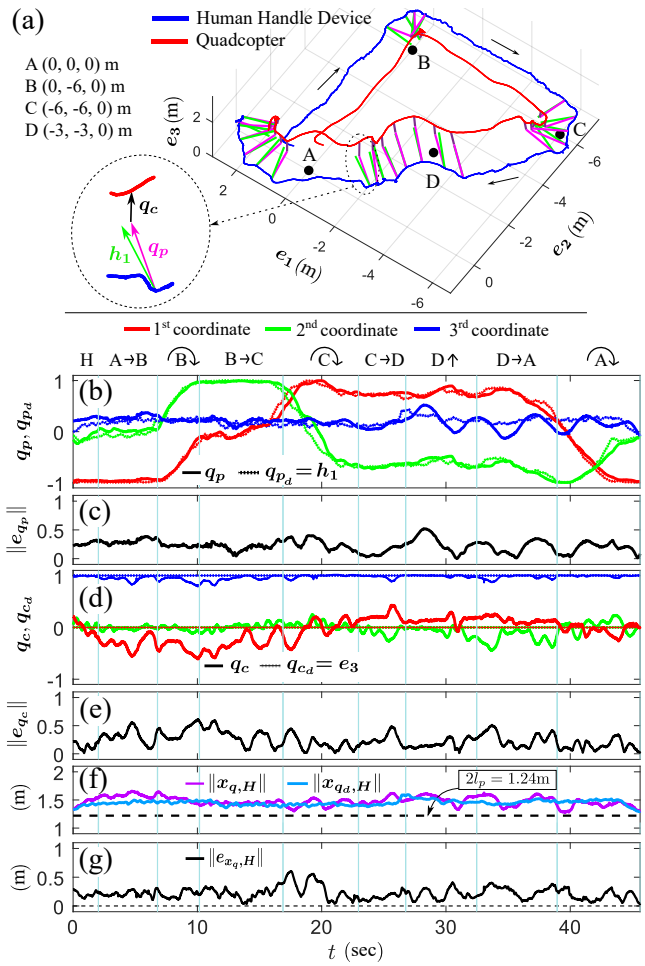


Fig. 6. Outdoor experimental results of a representative subject. (a) Three-dimensional trajectory traced by the quadcopter and *HHD*. The subject drives the system along $\boldsymbol{A}$-$\boldsymbol{B}$-$\boldsymbol{C}$-$\boldsymbol{A}$ path starting from point $\boldsymbol{A}$. Point $\boldsymbol{D}$ indicates the obstacle's position. The desired payload attitude, payload attitude, and cable attitude are shown at some intervals over the trajectory. (b) Payload's actual and desired attitude ($\boldsymbol{q_p}$ and $\boldsymbol{q}_{p_d}$) are shown in terms of coordinates. (c) Magnitude of payload attitude error, $\|\boldsymbol{e}_{q_p}\|$. (d) Cable's actual and desired attitude ($\boldsymbol{q_c}$ and $\boldsymbol{q}_{c_d}$) are shown in terms of coordinates. (e) Magnitude of cable attitude error, $\|\boldsymbol{e}_{q_c}\|$. (f) Actual and desired quadcopter's distance w.r.t. point $\boldsymbol{H}$, i.e., $\|\boldsymbol{x}_{q,H}\|$ and $\|\boldsymbol{x}_{q_d,H}\|$ respectively. (g) Magnitude of error between the actual and desired quadcopter's position w.r.t. point $\boldsymbol{H}$, $\|\boldsymbol{e}_{x_q,H}\|$.

almost all sections of the trajectory for all subjects, as shown in Fig. 7 (b). Occasionally, for example for subject 2 during section $\boldsymbol{A} - \boldsymbol{B}$, its value was slightly lower than $2l_p$. Thus, a safe distance was maintained, and the system enabled safe maneuvering during the experiment.

The tracking of payload and cable attitudes during the experiment are shown in Figs. 6 (b & d) for the representative subject. The adopted strategy for the experiment was to keep the cable vertically taut, i.e., constant $\boldsymbol{q}_{c_d} = \boldsymbol{e_3}$. At the same time, the human operator decides the payload attitude, i.e., variable $\boldsymbol{q}_{p_d} = \boldsymbol{h}_1$. The results show good tracking of $\boldsymbol{q}_{c_d}$ and $\boldsymbol{q}_{p_d}$. The error magnitudes in payload and cable attitude are shown in Figs. 6 (c & e) for the representative subject, and their root-mean-square values, $\rho(\|\boldsymbol{e}_{q_{(\cdot)}}\|)$, are presented in Figs. 7 (c & d) for the different sections of the trajectory for all subjects. As the operator varied $\boldsymbol{h}_1$ to execute the trajectory, the quadcopter varied its attitude to track the desired cable and payload attitudes. Specifically, the error values were large at

**IEEE Robotics and Automation Letters (RA-L) paper, presented at ICRA 2024, Yokohama, Japan. Cite as RA-L paper.**

**IEEE Robotics and Automation Letters (RA-L) paper, presented at ICRA 2024, Yokohama, Japan. Cite as RA-L paper.**

turns/obstacles and varied between subjects.

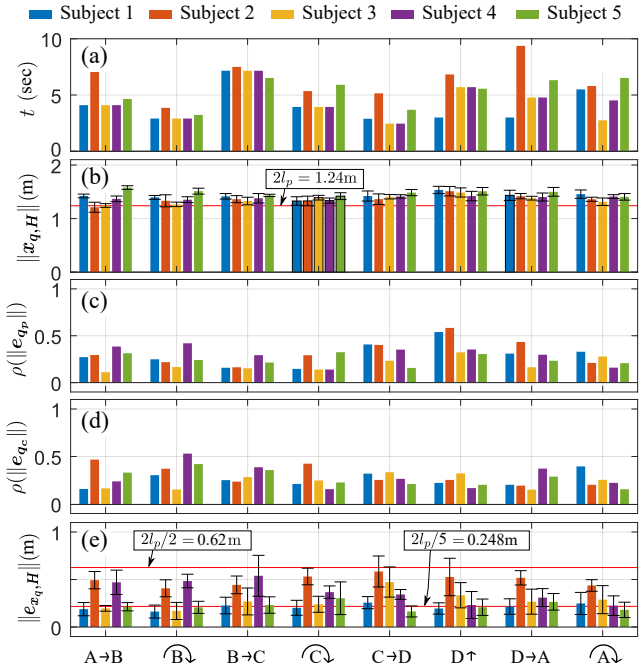


Fig. 7. Quantitative analysis of all subjects' experimental data while moving the system along all the sections. Plot (a) shows the time to complete the section. Plot (b) shows mean and standard deviation values of $\|\boldsymbol{x_{q,H}}\|$. Plots (c & d) show the root-mean-square of error magnitude in payload's and cable's attitude, i.e., $\rho(\|\boldsymbol{e_{q_{(\cdot)}}}\|)$ respectively. Plot (e) shows mean and standard deviation values of $\|\boldsymbol{e_{x_{q,H}}}\|$.

The cumulative effect of errors in cable and payload attitudes are presented using parameter $\|\boldsymbol{e_{x_q,H}}\|$, which measures the magnitude of the quadcopter's position error w.r.t. point $\boldsymbol{H}$. It is plotted in Fig. 6 (g) for the representative subject, and its mean and standard deviation values are plotted in Fig. 7 (e) for the different sections of the trajectory for all subjects. For most of the trajectory, the $\|\boldsymbol{e_{x_q,H}}\|$ values were small, less than one-fifth of the payload's length ($2l_p/5$), refer to Fig. 7 (e). For some subjects, during specific trajectory sections, the $\|\boldsymbol{e_{x_q,H}}\|$ values were higher, reaching half the payload's length ($l_p$) mark. The controller's gains can be tuned further to maintain small values of $\boldsymbol{e_{x_q,H}}$. Overall, these results demonstrate that the implemented human-quadcopter physical manifestation allowed the operator to execute multiple turns and avoid obstacles in outdoor settings without onboard localization.

## V. DISCUSSIONS AND CONCLUSIONS

The current work demonstrates a physical human aerial robot interaction (*pHARI*) modality in the outdoor setting. The successful experiments with five novice subjects establish the feasibility of proposed paradigms in applications such as impromptu material handling tasks at warehouses and construction sites.

Most of the *pHARI* work hitherto has been carried out in indoor settings [16]–[21]. A combination of sensors, including motion capture systems, onboard cameras or visual odometry, force-torque sensor, etc., have been used to localize the human and robot during the experiment and estimate the human commands and state feedback for the controller. To this end, the direct involvement of the human in maneuvering the system as part of the presented *pHARI* modality eliminated the need for onboard localization. For outdoor flights, two custom build sensor systems were designed and deployed onboard to accurately estimate human commands and state feedback. The cable attitude measurement device, *CAMD*, has a similar working approach as the device in [28], [29]. Notably, a unique design has been proposed for *HHD* to estimate human commands. As these devices use encoders, IMU, and microcontrollers, they are comparatively lightweight and require fewer computational resources.

Among the existing *HRI* works using aerial robots, the human operator administers the high-level commands either via teleoperation [5]–[13] or through external physical interaction [16], [18], [20], [21] with a self-sustained aerial robotic system. In contrast, the current work introduced a novel *pHARI* approach in which the human operator not only provides high-level commands but also engages in performing the collaborative payload transportation task. Essentially, the human operator lifts part of the payload and maneuvers it along a path. The quadcopter acts like an assistive robot, similar to cooperative ground robots in works [22], [23], which also lifts and stabilizes the payload during transportation. Moreover, the presented human-quadcopter experiments establish that a human need not know how to fly an aerial robot to execute such cooperative tasks.

Aerial transportation of cable-suspended payload by multiple quadcopters has been widely studied in the literature [11]–[13], [18], [21], [30]. Typically, the developed control framework stabilizes the system about specific hovering conditions, where depending upon the desired configuration the payload weight sharing is sought among the agents. In this context, the presented physical collaboration transportation framework sought equal payload weight sharing between the human and quadcopter. Further, the quadcopter is controlled to keep the cable vertically taut and maintain the payload attitude according to the human commands ($\boldsymbol{q_{p_d}} = \boldsymbol{h_1}$). Such a framework allowed the operator to adjust the system configuration on the go to execute the turns and avoid obstacles while the quadcopter ensured a safe and smooth flight.

The current work implements a state-feedback control law to successfully execute the proposed collaborative strategy of safely assisting humans during the task. However, one of the limitations of the current work is in utilizing the same quadcopter's controller gain $\boldsymbol{\mathcal{K}_q}$ to control the cable and payload attitudes. This resulted in the varied tracking performance of the cable and payload attitude between subjects during experiments. Even though the gain matrix $\boldsymbol{\mathcal{K}_q}$ was tuned experimentally to address a diverse range of perturbations, incorporating an appropriate human action model is required for consistent tracking performance between subjects. In various human interaction works in literature [16]–[21], human impedance is typically modeled as a spring-mass-damper system, and admittance control approaches are used. Further, the human gain matrix $\boldsymbol{\mathcal{K}_h}$ can be adopted using approaches presented in [31], which develop human-like controllers to interact with unknown environments. It is therefore proposed

**IEEE Robotics and Automation Letters (RA-L) paper, presented at ICRA 2024, Yokohama, Japan. Cite as RA-L paper.**

to include the human input modeling to compute the feedback gain matrix in our future work. Such modeling will enable a former stability proof and robust tracking performance.

## APPENDIX

### A. Expressions for Matrices $M, N$, and $L$

As the desired attitude of the cable is considered $e_3$, i.e., $q_{c_d} = e_3$, the obtained linearized equations corresponding to the third element of $\dot{\xi}_c$ and $\delta\dot{\omega}_c$ become zero. Thus, a matrix $L = \begin{bmatrix} e_1 & e_2 \end{bmatrix} \in \mathbb{R}^{3\times 2}$ is introduced in the state vector $\delta s$ to eliminate the third element of $\dot{\xi}_c$ and $\delta\dot{\omega}_c$ as given in Eq. (8). Accordingly, the expressions for matrices $M$ and $N$ are given as follows.

$$M = -A^{-1}B, \quad N = A^{-1}C, \tag{26}$$

where,

$$A = \begin{bmatrix} I_{8\times 8} & & 0_{8\times 8} & & \\ & & A_{44} & A_{45} & A_{46} \\ 0_{8\times 8} & & A_{54} & A_{55} & A_{56} \\ & & A_{64} & A_{65} & A_{66} \end{bmatrix}, \; C = \begin{bmatrix} 0_{8\times 3} & 0_{8\times 3} \\ I_{3\times 3} & I_{3\times 3} \\ 0 & 2l_p q_{p_d} \\ 0 & L^T l_c \widehat{e}_3 \end{bmatrix}$$

$$B = \begin{bmatrix} 0_{3\times 3} & 0_{3\times 3} & 0_{3\times 2} & -I_{3\times 3} & 0_{3\times 3} & 0_{3\times 2} \\ 0_{3\times 3} & 0_{3\times 3} & 0_{3\times 2} & 0_{3\times 3} & B_{25} & 0_{3\times 2} \\ 0_{2\times 3} & 0_{2\times 3} & 0_{2\times 2} & 0_{2\times 3} & 0_{2\times 3} & I_{2\times 2} \\ 0_{3\times 3} & 0_{3\times 3} & 0_{3\times 2} & 0_{3\times 3} & 0_{3\times 3} & 0_{3\times 2} \\ 0_{3\times 3} & B_{42} & 0_{3\times 2} & 0_{3\times 3} & 0_{3\times 3} & 0_{3\times 2} \\ 0_{2\times 3} & 0_{2\times 3} & B_{53} & 0_{2\times 3} & 0_{2\times 3} & 0_{2\times 2} \end{bmatrix}_{16\times 16}$$

$A_{44} = (m_q + m_p)I_{3\times 3}$, $A_{45} = -(2m_q + m_p)l_p\widehat{q}_{p_d}$, $A_{46} = -m_q l_c \widehat{e}_3 L$, $A_{54} = (2m_q + m_p)l_p\widehat{q}_{p_d}$, $A_{55} = (4m_q + \frac{4}{3}m_p)l_p^2 I_{3\times 3}$, $A_{56} = -2m_q l_p l_c (e_3 q_{p_d}^T - (q_{p_d} \cdot e_3)I_{3\times 3})L$, $A_{64} = m_q l_c L^T \widehat{e}_3$, $A_{65} = -2m_q l_p l_c L^T (q_{p_d} e_3^T - (e_3 \cdot q_{p_d})I_{3\times 3})$, $A_{66} = m_q l_c^2 I_{2\times 2}$, $B_{25} = I_{3\times 3} - q_{p_d} q_{p_d}^T$ $B_{42} = (-(2m_q + m_p)l_p g((e_3 \cdot q_{p_d})I_{3\times 3} - q_{p_d} e_3^T) - 2l_p(q_{p_d} u_{q_d}^T - (u_{q_d} \cdot q_{p_d})I_{3\times 3}))$, $B_{53} = L^T((-m_q l_c g(I_{3\times 3} - e_3 e_3^T) - l_c(e_3 u_{q_d}^T - (u_{q_d} \cdot e_3)I_{3\times 3}))L$.

## REFERENCES


[1] Thomas B Sheridan. Human–robot interaction: status and challenges. *Human factors*, 58(4):525–532, 2016.

[2] Ildar Farkhatdinov, Jee-Hwan Ryu, and Jinung An. A preliminary experimental study on haptic teleoperation of mobile robot with variable force feedback gain. In *2010 IEEE Haptics Symposium*, pages 251–256, 2010.

[3] Luka Peternel, Nikos Tsagarakis, and Arash Ajoudani. Towards multi-modal intention interfaces for human-robot co-manipulation. In *2016 IEEE/RSJ International Conference on Intelligent Robots and Systems (IROS)*, pages 2663–2669, 2016.

[4] Ana C De Oliveira, James S Sulzer, and Ashish D Deshpande. Assessment of upper-extremity joint angles using harmony exoskeleton. *IEEE Transactions on Neural Systems and Rehabilitation Engineering*, 29:916–925, 2021.

[5] FJ Perez-Grau, R Ragel, F Caballero, A Viguria, and A Ollero. Semi-autonomous teleoperation of uavs in search and rescue scenarios. In *2017 International Conference on Unmanned Aircraft Systems (ICUAS)*, pages 1066–1074. IEEE, 2017.

[6] Werner Alexander *et al.* High-level teleoperation system for aerial exploration of indoor environments. *Frontiers in Robotics and AI*, page 95, 2019.

[7] Lee Jongseok *et al.* Visual-inertial telepresence for aerial manipulation. In *2020 IEEE International Conference on Robotics and Automation (ICRA)*, pages 1222–1229. IEEE, 2020.

[8] Ollero Anibal *et al.* The aeroarms project: Aerial robots with advanced manipulation capabilities for inspection and maintenance. *IEEE Robotics Automation Magazine*, 25(4):12–23, 2018.

[9] Huan Nguyen and Kostas Alexis. Forceful aerial manipulation based on an aerial robotic chain: Hybrid modeling and control. *IEEE Robotics and Automation Letters*, 6(2):3711–3719, 2021.

[10] Pratik Prajapati, Sagar Parekh, and Vineet Vashista. On-board cable attitude measurement and controller for outdoor aerial transportation. *Robotica*, 40(5):1650–1664, 2022.

[11] Pratik Prajapati, Sagar Parekh, and Vineet Vashista. On the human control of a multiple quadcopters with a cable-suspended payload system. In *2020 IEEE International Conference on Robotics and Automation (ICRA)*, pages 2253–2258, 2020.

[12] Andrea Tagliabue, Mina Kamel, Sebastian Verling, Roland Siegwart, and Juan Nieto. Collaborative transportation using mavs via passive force control. In *2017 IEEE International Conference on Robotics and Automation (ICRA)*, pages 5766–5773. IEEE, 2017.

[13] Carlo Masone, Heinrich H Bülthoff, and Paolo Stegagno. Cooperative transportation of a payload using quadrotors: A reconfigurable cable-driven parallel robot. In *2016 IEEE/RSJ International Conference on Intelligent Robots and Systems (IROS)*, pages 1623–1630. IEEE, 2016.

[14] Parastoo Abtahi, David Y Zhao, Jane L E, and James A Landay. Drone near me: Exploring touch-based human-drone interaction. *Proceedings of the ACM on Interactive, Mobile, Wearable and Ubiquitous Technologies*, 1(3):1–8, 2017.

[15] Salaan Carl John *et al.* Uav with two passive rotating hemispherical shells for physical interaction and power tethering in a complex environment. In *2017 IEEE International Conference on Robotics and Automation (ICRA)*, pages 3305–3312. IEEE, 2017.

[16] Federico Augugliaro and Raffaello D'Andrea. Admittance control for physical human-quadrocopter interaction. In *2013 European Control Conference (ECC)*, pages 1805–1810. IEEE, 2013.

[17] Marco Tognon, Rachid Alami, and Bruno Siciliano. Physical human-robot interaction with a tethered aerial vehicle: Application to a force-based human guiding problem. *IEEE Transactions on Robotics*, 37(3):723–734, 2021.

[18] Matthew Romano, Anne Ye, John Pye, and Ella Atkins. Cooperative multilift slung load transportation using haptic admittance control guidance. *Journal of Guidance, Control, and Dynamics*, 45(10):1899–1912, 2022.

[19] Mike Allenspach, Yash Vyas, Matthias Rubio, Roland Siegwart, and Marco Tognon. Human-state-aware controller for a tethered aerial robot guiding a human by physical interaction. *IEEE Robotics and Automation Letters*, 2022.

[20] Amr Afifi, Mark van Holland, and Antonio Franchi. Toward physical human-robot interaction control with aerial manipulators: Compliance, redundancy resolution, and input limits. In *2022 International Conference on Robotics and Automation (ICRA)*, pages 4855–4861. IEEE, 2022.

[21] Xinyang Liu, Guanrui Li, and Giuseppe Loianno. Safety-aware human-robot collaborative transportation and manipulation with multiple mavs. *arXiv preprint arXiv:2210.05894*, 2022.

[22] Luka Peternel, Nikos Tsagarakis, and Arash Ajoudani. Towards multi-modal intention interfaces for human-robot co-manipulation. In *2016 IEEE/RSJ international conference on intelligent robots and systems (IROS)*, pages 2663–2669. IEEE, 2016.

[23] Alexander Mörtl, Martin Lawitzky, Ayse Kucukyilmaz, Metin Sezgin, Cagatay Basdogan, and Sandra Hirche. The role of roles: Physical cooperation between humans and robots. *The International Journal of Robotics Research*, 31(13):1656–1674, 2012.

[24] Francesco Bullo and Andrew D Lewis. *Geometric control of mechanical systems: modeling, analysis, and design for simple mechanical control systems*, volume 49. Springer, 2019.

[25] Guofan Wu and Koushil Sreenath. Variation-based linearization of nonlinear systems evolving on $so(3)$ and $\mathbb{S}^2$. *IEEE Access*, 3:1592–1604, 2015.

[26] Taeyoung Lee, Melvin Leok, and N Harris McClamroch. Control of complex maneuvers for a quadrotor uav using geometric methods on se (3). *arXiv preprint arXiv:1003.2005*, 2010.

[27] Lung-Wen Tsai. *Robot analysis: the mechanics of serial and parallel manipulators*. John Wiley & Sons, 1999.

[28] Yunfan Ren, Jianheng Liu, Haoyao Chen, and Yunhui Liu. Vision-encoder-based payload state estimation for autonomous mav with a suspended payload. In *2021 IEEE/RSJ International Conference on Intelligent Robots and Systems (IROS)*, pages 9632–9638. IEEE, 2021.

[29] Morten Bisgaard, Anders la Cour-Harbo, Eric N Johnson, and Jan Dimon Bendtsen. Vision aided state estimator for helicopter slung load system. *IFAC Proceedings Volumes*, 40(7):425–430, 2007.

[30] Roberto C Sundin, Pedro Roque, and Dimos V Dimarogonas. Decentralized model predictive control for equilibrium-based collaborative uav bar transportation. In *2022 International Conference on Robotics and Automation (ICRA)*, pages 4915–4921. IEEE, 2022.

[31] Chenguang Yang, Gowrishankar Ganesh, Sami Haddadin, Sven Parusel, Alin Albu-Schaeffer, and Etienne Burdet. Human-like adaptation of force and impedance in stable and unstable interactions. *IEEE transactions on robotics*, 27(5):918–930, 2011.